Pre-processing of Remotely Sensed Imagery

Peter Bunting

Abstract A common obstacle to the use of remote sensing data for nature conservation is the difficulty in obtaining or generating data that are pre-processed to a standard that gives confidence in their subsequent use. Such processing is essential in order to facilitate physical measurement (e.g., of temperature, surface reflectance, height) and compare data (e.g., reflectance or radar backscatter) acquired for different dates or areas. For optical and radar data, this pre-processing includes orthorectification, calibration, atmospheric and topographic correction and, in the case of LiDAR, ground return classification and surface height retrieval. This chapter therefore provides an overview of the common pre-processing steps that are undertaken or needed in order to create what has been recently termed an analysis ready data (ARD) product. Increasingly, such products are being provided routinely to minimize the effort of data users but knowledge of how this is achieved is important in determining the integrity and understanding the use of the data. The information provided should help users to identify, select and use data with confidence or to perform their own processing of the raw data.

Keywords Earth observation • Optical • Radar • Lidar • Preprocessing • Atmosphere • Topography • Geometric correction

Introduction

Pre-processing of all remotely sensed imagery, whether airborne or spaceborne, first involves a geometric correction, with this ensuring accurate spatial location of datasets on the Earth's surface (Lillesand et al. 2004). Standardization to a scientific unit is then undertaken such that the data are comparable to that acquired from the same or different sensors (Analysis Ready Data; ARD), with this including calibration of optical data to radiometric units and atmospheric correction to units of reflectance, transformation of Synthetic Aperture Radar (SAR) data to backscatter and other

P. Bunting (✉)
Earth Observation and Ecosystem Dynamics Group, Department of Geography and Earth Sciences, Aberystwyth University, Aberystwyth SY23 3DB, UK
e-mail: pfb@aber.ac.uk

R. Díaz-Delgado et al. (eds.), *The Roles of Remote Sensing in Nature Conservation*,
DOI 10.1007/978-3-319-64332-8_3

Table 1 Standard processing levels and products that could be requested

Sensor	Type	Typical Pre-processing	Derived products
Optical	Spaceborne multispectral	Surface reflectance using a modeled atmosphere.	–
	Airborne multispectral	Surface reflectance using ground targets and/or ground reflectance targets.	–
	Airborne Hyperspectral	Surface reflectance using ground targets and/or ground reflectance targets.	–
	UAV multispectral	Surface reflectance using ground reference targets	Stereo-derived Digital Surface Model (DSM).
LiDAR	Airborne (small footprint)	Ground returns classified and return height above surface defined	Digital Terrain Model (DTM), Digital Surface Model (DSM) and Canopy Height Model (CHM).
SAR	Spaceborne/airborne	Normalised radar cross section (σ^0), commonly displayed in decibels (dB).	–

units or classification of LiDAR ground returns to surface elevation (Table 1). The generation of ARD is often performed by the data providers, reseller or consultant specialists with knowledge of the algorithms and procedures but where in-house expertise and software are available, costs can be reduced. The following sections discuss each of these products and pre-processing routines with specific guidance on the selection of data request specifications and implications of pre-processing decisions.

Geometric Correction of Airborne and Spaceborne Data

In many instances, particularly for modern spaceborne and airborne LiDAR acquisitions, high-quality geometric correction is provided by the data provider (Shan and Toth 2009). However, there are several considerations when undertaking or contracting geometric correction of data.

For airborne datasets, the quality of the geometric correction is defined by the accuracy of the 3-dimensional (3-D) position and orientation of the aircraft during the acquisition (Schlapfer and Richter 2002). An inertial motion unit (IMU) and differential Global Positioning System (dGPS) measure the position and orientation of the aircraft and it is the frequency and accuracy of these measurements that need to be considered when commissioning airborne data acquisitions. For satellite datasets, the location of the satellite and the parameters of the acquisition are key and

should be provided with the image data by the data provider in a standard format (format is commonly customised to each data provider) for ingestion to the appropriate processing software (e.g., Schwind et al. 2009).

Once the location of the instrument (whether aircraft or satellite) has been defined and recorded, a model of the acquisition is defined in software. LiDAR directly measures the 3-D component of the environment but for optical (e.g., multispectral and hyperspectral) and SAR, a Digital Elevation Model (DEM) is required to perform an orthorectification. Orthorectification removes the geometric distortion from the image acquisition (i.e., being captured from a single point) such that there is a common viewpoint or datum plane (Fig. 1; Lillesand et al. 2004). However, at extreme viewing angles, full correction may not be possible because of regions of missing data (i.e., shadowing) while the resolution of the DEM used for the correction needs to be appropriate for the scale of features within the scene. For example, where an orthorectification is being performed on imagery where individual isolated trees or buildings are visible, then the DEM needs to have a 3D representation of these features for the imagery to be fully orthorectified. Where a suitably high-resolution DEM has not been used and the viewing geometry differed between

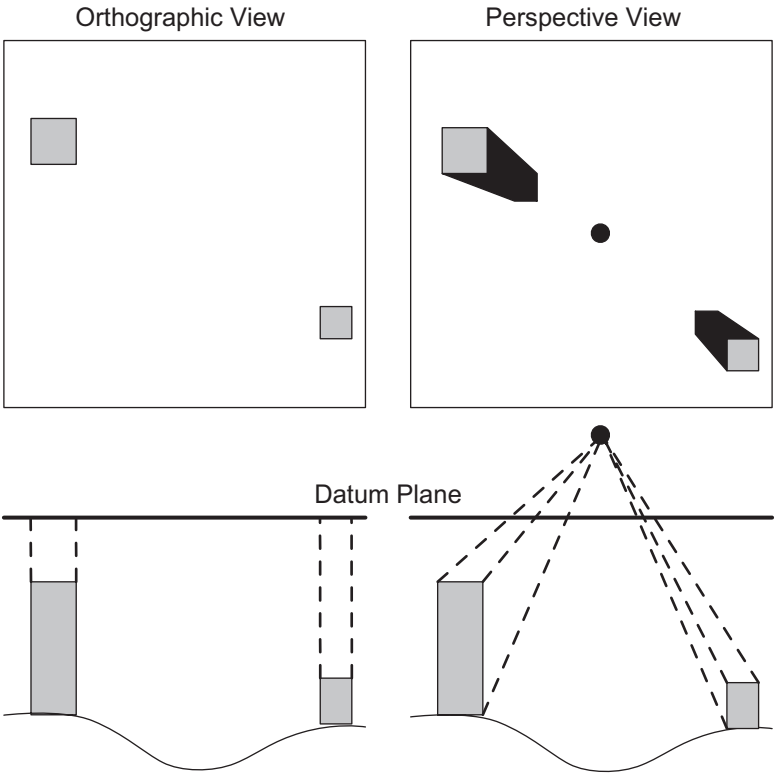

Fig. 1 Orthorectification corrects the geometry of the image with respect to the datum plane

scenes, pixel misalignments between images might be expected for these small 3D features (e.g., trees, buildings, etc.).

While recent imagery acquired from larger manned platforms has demonstrated a high degree of geometric quality, with standard and robust geometric correction routines developed, correction of data from the newer Unmanned Aerial Vehicles (UAVs or drone) platforms needs greater consideration and care. Specifically, because of the weight requirements of the UAV platforms, lighter and lower quality IMU and GPS units are fitted and therefore accuracy is lowered. Additionally, as the acquisition process involves a large number of images, with each covering small areas, an image matching process is required to create a single mosaicked image. The overlapping regions of these images can also be used to build a high-resolution DEM for the area, which can be subsequently utilised for the orthorectification of the image mosaic (Jhan et al. 2016). It is recommended that ground control points (GCPs) are acquired for ground targets unless differential GPS (dGPS) system with real-time kinematic GNSS (RTK) or post-processed kinematic (PPK) are used during the UAV acquisition. Where GCPs are used, these will subsequently need to be identified within the UAV imagery, which can be a time-consuming process. However, with the latest RTK and PPK enabled GPS systems, pixel 9 locational accuracies are commonly within ±5 cm in the x and y axis' and ±10 cm in the z axis without the need for manual intervention.

Optical Data

Optical sensors measure the amount of light that is reflected from the ground surface. However, between the ground surface and the sensor, there is an atmosphere that contributes to the measured reflectance. There are various pre-processing stages that can be applied, but removing the atmospheric and bidirectional effects is key to providing a comparable and full standardised product. However, bidirectional effects are commonly not corrected for (Nagol et al. 2015), as it can be difficult to fully define the bidirectional reflectance distribution function (BRDF). For high-resolution data, knowledge of the ground surface orientation at comparable resolutions or better is commonly not available. Bidirectional reflectance is the change in the amount of light reflected due to the geometry of the acquisition, which is attributable to differences in the solar angles (e.g., with season and time of day) and sensor geometry (i.e., view angle of the sensor). These angles are with respect to the ground surface, which themselves are defined with respect to the pixel resolution of the imagery acquired. Therefore, for very high-resolution (VHR datasets, such as acquired from a UAV), the orientation of individual leaves might need to be known to correct for bidirectional effects within the image.

When energy (in this case, light) interacts with a medium, reflection, transmission or absorbance occurs. For example, as light from the sun interacts with plant leaves, a proportion of this is reflected and transmitted and the remaining is absorbed. It is the reflected component that is measured by remote sensing instruments.

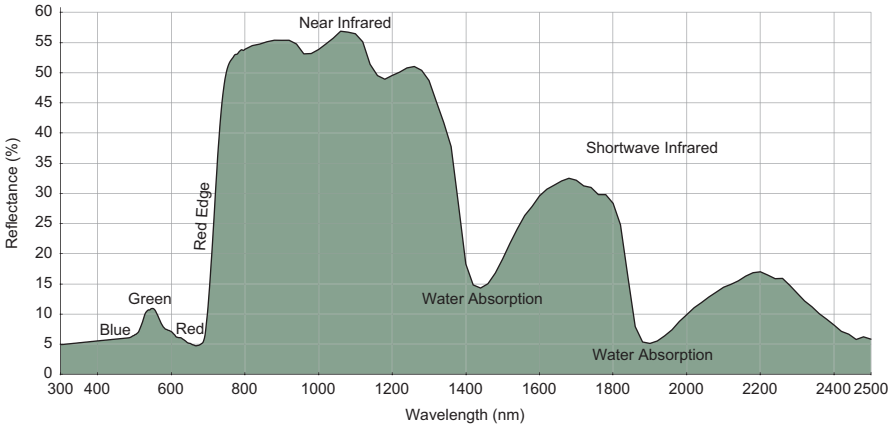

Fig. 2 Typical reflectance curve for vegetation from a field spectrometer sampling at 1 nm intervals from 300–2500 nm

The percent or proportion of energy reflected throughout the electromagnetic spectrum is commonly referred to as the reflectance curve (Fig. 2).

The spectral curve for vegetation in Fig. 2 has been measured at a very high spectral resolution (i.e., sampling at intervals every 1 nanometer; nm). Commonly, multi-spectral imagers are used for remote data acquisition and the resolution at which the reflectance of the surface is measured is therefore at a much lower spectral resolution. The resolution and sensitivity of the sensor is defined by its spectral response functions (e.g., Fig. 3a and b), with one available for each image band captured. When considering the use of an instrument for a particular application, it is the position (i.e., wavelength) of the peak of maximum sensitivity and the width of the peak that defines the measured reflectance response. The spectral response is commonly modeled as a Gaussian and therefore is quoted as the wavelength of the peak and a full-width half maximum (FWHM) of the response sensitivity. When comparing field-derived ground spectra (e.g., Fig. 2) to the signal measured by satellite or aircraft sensors, the spectral response functions need to be applied to the ground measurement (e.g., Fig. 3c).

Radiance

Optical data recorded in a particular wavelength region (λ), and obtained from the data provider, should be given in units of radiance ($L_\lambda W\ m^{-2}\ sr^{-1}\ \mu m^{-1}$). In order to compress (i.e., reduce the file size), the image is typically provided with a gain and offset to convert the pixel value, commonly referred to as the digital number (DN), to radiance where:

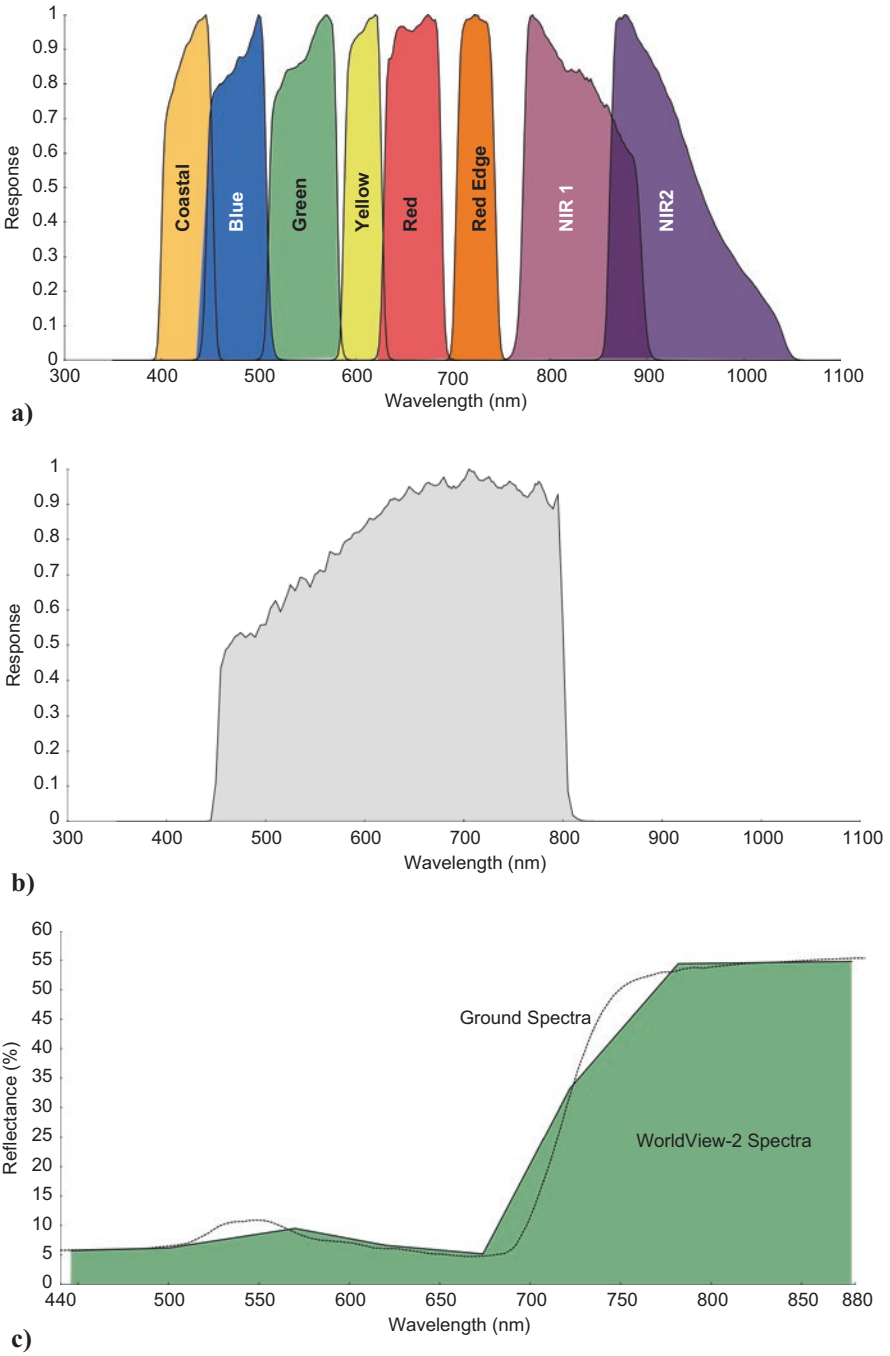

Fig. 3 (**a**) Multi-spectral image bands spectral response functions and (**b**) the panchromatic response functions for Worldview-2 data as an example. (**c**) The reflectance curve for vegetation (440–880 nm) resampled using the Worldview-2 multi-spectral functions

$$\mathbf{L}_{\lambda} = \left(\text{gain} \times \text{DN}\right) + \text{offset}$$

Before proceeding with further processing, these gains and offsets should be applied to your imagery, such that each pixel value represents the radiance measured by the sensor.

For UAV imagery mosaicked from many individual images, care is needed where the camera has used different exposure parameters (i.e., ISO, aperture, shutter speed). The pixels values correlating to the amount of radiance will differ and converting to radiance will not be possible once mosaicked. If correction is required for UAV imagery, then the camera parameters need to be known and ideally should be constant throughout the flight. Additionally, the camera needs to be calibrated to relate the digital number (DN) value of the camera to radiance.

At Sensor Radiance

At sensor reflectance, also referred to as top of atmosphere (TOA) reflectance, is a standard and easily calculated ratio of the incoming radiant energy (light) from the sun (ESUN) and the corresponding radiance measured by the sensor. The radiance measured at the sensor differs from the incoming signal due to the reflectance of the Earth surface and the atmosphere (or part of the atmosphere) the signal has transmitted through. Although providing a standard measure and common range of values (0–1), the reflectance measurement includes the reflectance from the atmosphere and the ground surface and therefore images taken at different times are not directly comparable. At sensor reflectance is calculated as:

$$\rho_{\lambda} = \frac{\pi \cdot \mathbf{L}_{\lambda} \cdot \mathbf{d}^{\mathbf{2}}}{\mathbf{ESUN}_{\lambda} \cdot \mathbf{cos}\theta_{\mathbf{S}}}$$

where λ is the wavelength, ρ_{λ} is the spectral (at sensor or top of atmosphere) reflectance for wavelength λ, L_{λ} is the spectral radiance (W m^{-2} sr^{-1} μm^{-1}), d is the Earth-Sun distance in astronomical units, $ESUN_{\lambda}$ is the mean solar exoatmospheric irradiance in units of W m^{-2} μm^{-1} and θ_s is the solar zenith angle.

Surface Reflectance

Surface reflectance, also called 'bottom of atmosphere reflectance' is the ratio of incoming radiance (i.e., from the sun) with the radiance that is measured by the sensor without the atmospheric effect and should be equivalent to the signal measured if the sensor was at ground level or there was no atmosphere. To derive this

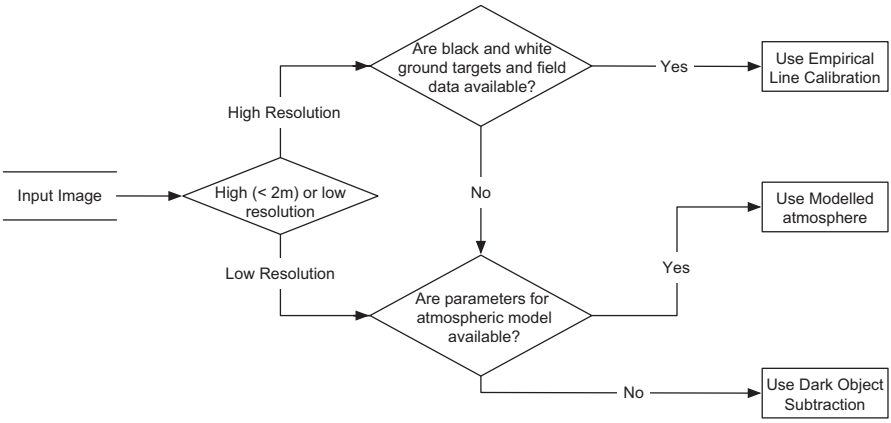

Fig. 4 Decision tree for which measure of atmospheric correction you should use

measurement, the effect of the atmosphere needs to be removed from the at sensor radiance measured at the sensor. There are a number of options (Fig. 4) for this.

The Empirical Line Calibration (Smith and Milton 2010) is commonly used to correct high-resolution airborne imagery but requires that ground data of bright and dark targets be captured at the time of the overflight. Dark Object Subtraction methods (Chavez 1988) are relatively simple and require relatively little inputs so can be easily applied to all image data but do not produce the most reliable and consistent results. It is, therefore, the method used when the others are not available. Modeled Atmospheric Correction Methods (Vermote et al. 1997; Masek et al. 2006) model reflection, absorption and scattering by the atmosphere and commonly used models include 6S (Vermote et al. 1997), LOWTRAN, MODTRAN, FLAASH, ATCOR and HYCOR. These models require many parameters to be known or estimated and can, therefore, be complex to apply. However, for lower resolution imagery or where ground spectra for targets are not available, it is the best solution. Further details on these approaches are provided in the following sections.

Empirical Line Calibration

An empirical line calibration is a simple process (Smith and Milton 2010) of collecting the ground reflectance of at least two targets that will be captured by the observing sensor, one that has a reflectance of 0% (or close to; i.e., black) and another with a reflectance of or near 100% (i.e., white). Additional targets of different shades of grey (i.e., levels of reflectance) can also be laid out to improve the reflectance estimates. The targets need to be at least three times the size of the image pixels (i.e., 1 m pixels requires at least a 3 × 3 m target) to ensure that more than one pure pixel of the target is acquired. However, larger targets producing more than one pure pixel at the pixel resolution are preferable. Another consideration is that the targets need to have a consistent reflectance across the full range of

wavelengths that the sensor is measuring. Once pure pixels have been identified, a linear regression of the image pixel values to the ground reflectance measurements for each wavelength is undertaken and the resulting relationship is used to convert the image to surface reflectance. Where multiple targets at each reflectance level are available, a validation of the relationship can be carried out.

Dark Object Subtraction (DOS)

A dark object subtraction (DOS; Chavez 1988) is built on a simple assumption that the darkest pixels within the scene have little or no surface reflectance and that the radiance measured by the sensor is from the atmosphere. Therefore, while assuming the atmosphere is consistent across the scene, subtracting that atmosphere component from the whole scene can be used to convert the at-sensor reflectance values to surface reflectance. This is performed independently for each of the image bands (i.e., wavelengths). However, there is a risk that the relative relationships between the image bands can vary.

Modeled Atmospheres

Modeling the atmosphere is the most common way in which imagery is atmospherically corrected but this requires a radiative transfer (RT) model and associated parameters, many of which are supplied in the image header file from the data provider (e.g., date and time of the acquisition). However, typically you, as the end-user, would perform this analysis through a software package that aids the parameterization (e.g., automatically parses the supplied header file or associated metadata), runs the atmospheric model and applies the model outputs to the image file. There are a number of software packages and models that support this analysis (Table 2), but they each only support a defined number of sensors. These lists are being updated on a regular basis. Additionally, some products and analysis steps may not be possible for all sensors and therefore functionality may not be equal across all sensors (e.g., cirrus cloud correction uses bands only provided by Sentinel-2 and Landsat-8 instruments).

More recently, there has been some effort to standardize these processing stages and levels (Claverie et al. 2015; Feng et al. 2013; Ju et al. 2012; Roy et al. 2010) for the Landsat and Sentinel-2 imagery. The United States Geological Survey (USGS) is already supplying the Landsat archive (TM, ETM+, OSL) as an atmospherically corrected product (Masek et al. 2006) and, in time, there may be a similar service for Sentinel-2 imagery.

For the Second Simulation of the Satellite Signal in the Solar Spectrum (6S; Vermote et al. 1997) model (others models are similar), the parameters needed are given in Table 3. The sensor configuration and position parameters are well defined and known so these can be parameterized using the image header information. However, the parameters associated with the atmosphere at the time of the acquisition, specifically

Table 2 List of software packages for applying an atmospheric correction using a modeled atmosphere

Software	RT Model	Sensors	License
ATCOR-4[a] (airborne)	MODTRAN	Many – see website	Commercial
ATCOR-3[b] (satellite)	MODTRAN	Many – see website	Commercial
FLAASH[c]	MODTRAN	Many – see website	Commercial
LEDAPS[d]	6S	Landsat (TM, ETM+)	Free but closed source
SEN2COR[e]	MODTRAN	Sentinel-2	Free but closed source
ARCSI[f]	6S	Landsat (MSS, TM, ETM+, OLI), Rapideye, SPOT5, SPOT6, SPOT7, WorldView-2, WorldView-3, Pleiades, Sentinel-2	Free and Open Source

[a]www.rese-apps.com/software/atcor-4-airborn
[b]www.rese-apps.com/software/atcor-3-satellites
[c]www.harrisgeospatial.com/docs/FLAASH.html
[d]ledaps.nascom.nasa.gov
[e]step.esa.int/main/third-party-plugins-2/sen2cor/
[f]www.rsgislib.org/arcsi

the aerosol optical depth (AOD) and the total amount of water in a vertical path through the atmosphere (water vapour), are unknown and need to be provided by the user or estimated from the image for a more accurate atmospheric correction. The sensor and surface altitude parameters are defining the length of the path through the atmosphere that the signal being measured has taken (Fig. 5). The more atmosphere the signal passes through to the sensor, the larger the atmospheric effect which needs to be removed from the image (Fig. 5c).

For the dynamic components of the atmosphere, specifically the AOD and water vapour, there are various sources of information and methods that attempt to estimate those parameters from the image data itself (e.g., Masek et al. 2006). These parameters can vary over short temporal and spatial baselines while the quality of the atmospheric correction is highly sensitive (Fig. 6) to the correct estimation of these parameters. They also vary as a function of the wavelength.

The AOD is correlated with visibility (in km), and the two can be transformed from one another using the following relationship,

$$\mathrm{AOD} = \frac{3.9449}{\mathrm{vis}} + 0.08498$$

There are three main sources of AOD for parameterisation of the atmospheric model; (a) ground measurements, (b) estimates from a third party satellite or (c) estimates from the image being corrected. As the AOD varies over short temporal and spatial baselines (Wilson et al. 2014), estimates from the image being corrected will be the most reliable, both spatially and temporally, and hence this is the pre-

Table 3 Parameters for the 6S model

Parameter	Description	Known
Solar zenith	The zenith angle of the sun with respect to the earth surface for the area of acquisition.	✓
Solar azimuth	The azimuth angle of the sun with respect to the earth surface for the area of acquisition.	✓
Sensor zenith	The zenith angle of the sensor with respect to the earth surface for the area of acquisition.	✓
Sensor azimuth	The azimuth angle of the sensor with respect to the earth surface for the area of acquisition.	✓
Acquisition date and time	The exact date and time of the acquisition.	✓
Centre point of scene (lat, long)	The point on the Earth's surface for where the model is being run.	✓
Altitude of sensor	The height of the sensor above the Earth's surface.	✓
Altitude of ground surface	The height above sea level of the ground surface being measured.	✓
Atmospheric profile	The vertical distribution of the atmospheric layers at a given altitude with pressure, temperature and water vapour and ozone at that layer. However, this is commonly generalised to standard profiles for tropical, mid-latitude summer, mid-latitude winter, sub-arctic summer, sub-arctic winter. Standardised profiles can be automatically selected based on time and location.	✗ (✓)
Water vapour	The total amount of water in a vertical path through the atmosphere (in g/cm^2).	✗
Ozone	The total amount of ozone in a vertical path through the atmosphere (in cm-atm).	✗
Aerosol profile	The proportion of water-like, dust-like, oceanic-like and soot-like aerosol partials in the atmosphere. However, this is commonly generalised to standard profiles for continental, maritime, urban, desert and biomass burning. Standardised profiles can be automatically selected.	✗ (✓)
Aerosol optical depth (AOD)	The total amount of AOD in the vertical path through the atmosphere at 550 nm.	✗

ferred option. However, estimating the AOD from the image data requires some assumptions to be made to derive some estimates of the surface reflectance of the visible image bands and considerable computing resource to invert (at least partially) an atmospheric model.

Ground measurements, using a sun photometer, provide very accurate measures of AOD but these are point measurements and therefore not necessarily representative of the whole scene. Additionally, because of the sparse nature of the ground measurements, it is unlikely that data will be available for the image being processed. Some weather stations provide visibility data (e.g., in the UK) but again these are point measurements and not available everywhere.

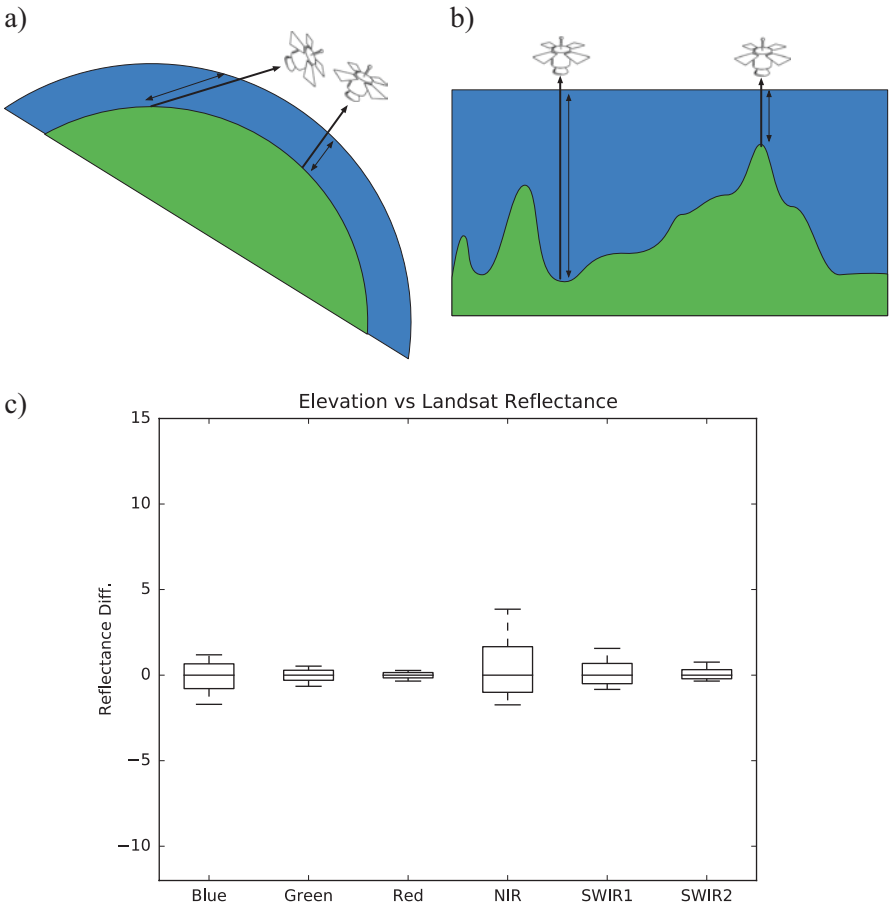

Fig. 5 Changes in the distance of the path through the atmosphere due to (a) sensor angular geometry and (b) surface altitude, which results in a variation in the outputted reflectance without appropriate correction (c) an example for the Landsat TM bands, where elevation varies from 0–5000 m

There are a number of satellite-based AOD products, primarily those derived from MODIS (Green et al. 2009). However, these products are produced at low spatial resolution (e.g., 1 km) and are generally not obtained at the same time as the image to be corrected. Furthermore, the downloading and processing of extra third party data is potentially a significant overhead for the correction of individual images. Table 4 provides an overview and reference to sources and algorithms for the retrieval of AOD.

For the correction of **atmospheric water**, there are a number of sources for water vapor within the vertical path (Table 5). The most commonly used sources are from third party satellites such as the MODIS. However, average climate data and ground-based measurements have also been used.

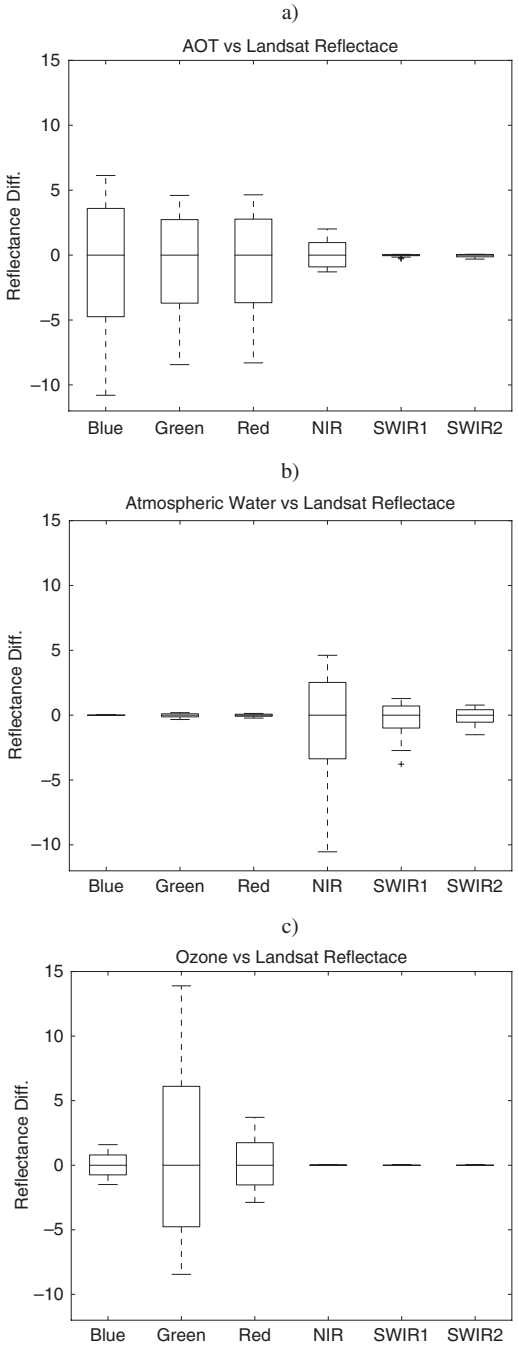

Fig. 6 Reflectance difference for Landsat TM bands with respect varying the following parameters in 6S (**a**) AOD (0.05–1.5). (**b**) vertical water column (1–15 g/cm^2) and (**c**) Ozone (0–5 cm-atm)

Table 4 Sources of measures of AOD

Source	Description
AERONET[a]	A network of sun photometers providing AOD measurements globally.
UK Meteorological Office (MIDAS)[b]	Integrated Data Archive System (MIDIS); specific to the UK, the Met Office makes ground measurements publically available.
MODIS[c]	Satellite-based measurement of AOD at 550 nm; available for free download.
LEDAPS[d]	Estimates of AOD for Landsat using dense dark vegetation (DDV) targets and relationships with the SWIR to visible wavelengths.
ARCSI[e]	Multiple algorithms, including the DDV method, but primarily uses a DOS based method to estimate surface reflectance in the blue wavelengths used for inversion.
SEN2COR[f]	Estimates AOD for Sentinel-2 using dense dark vegetation (DDV) targets and relationship from the SWIR to visible wavelengths.
Frantz et al. (n.d.)	Time series analysis to identify persistently dark targets that are used for AOD inversion.

[a]http://aeronet.gsfc.nasa.gov
[b]http://catalogue.ceda.ac.uk/uuid/220a65615218d5c9cc9e4785a3234bd0
[c]http://modis-atmos.gsfc.nasa.gov/MOD04_L2/
[d]http://ledaps.nascom.nasa.gov
[e]http://www.rsgislib.org/arcsi
[f]http://step.esa.int/main/third-party-plugins-2/sen2cor/

Table 5 Sources of measures of atmospheric water

Source	Description
MODIS[a]	Satellite-based measurement of total column water vapour. Freely available download.
Global precipitation measurement (GPM)[b]	NASA owned satellite that includes instruments for the measurement of total column water vapour.
AMSR-2[c]	JAXA owned satellite that includes instruments for the measurement of total column water vapour.
Seasonal average[d]	Where satellite estimates are not available for that date of acquisition Frantz et al. (n.d.) uses a local average.

[a]http://modis-atmos.gsfc.nasa.gov/MOD05_L2
[b]http://www.nasa.gov/mission_pages/GPM/main; Draper et al. (2015)
[c]http://suzaku.eorc.jaxa.jp/GCOM_W
[d]Frantz et al. (n.d.)

Table 6 Data and tools for establishing atmospheric ozone levels

TOMS	http://ozoneaq.gsfc.nasa.gov/data/toms/
GOME	http://www.ospo.noaa.gov/Products/atmosphere/gome/gome-A.html
OMI	http://neo.sci.gsfc.nasa.gov/view.php?datasetId=AURA_OZONE_E
NASA Ozone map tool	http://ozoneaq.gsfc.nasa.gov/tools/ozonemap/

As with water, **ozone** is commonly sourced externally from sensors such as NASA's Total Ozone Mapping Spectrometer (TOMS; 1978–2005) and ESA's Global Ozone Monitoring Experiment (GOME; 1996 to 2011). The Ozone Monitoring Instrument (OMI) has continued the time series of TOMS data since 2004 until the present. The download sites for these data are listed in Table 6, which also includes the NASA Ozone map tool that can be used to find the value of ozone from 1978 to the present based on TOMs and OMI data through a single interface.

Light Detection and Ranging (LiDAR)

Overview of Products and Software

Small footprint LiDAR data acquired via airborne platforms, primarily manned flights. However, more recently, there are small UAV octocopter based systems available (e.g., yellowscan; http://www.yellowscan.fr). LiDAR directly measures the 3D structure of a surface by way of a 3D point cloud, where other than the points returned from the same pulse, the topology of the point cloud is unknown (i.e., each pulse is independent). Multiple returns from a single fired pulse are only recorded for 'soft' targets such as vegetation (Fig. 7a) or the edges of hard targets, such as buildings (Fig. 7b). Multiple returns occur where a target causing the reflection back to the sensor is smaller than the footprint of the LiDAR. For a small footprint LiDAR, the footprint is typically around 20–30 cm. There are also so-called large-footprint LiDAR systems (e.g., ICESAT; Zwally et al. 2002), where the footprint is measured in metres, but these are not considered within this Chapter. Please refer to Shan and Toth (2009) for a discussion of large-footprint systems and their applications.

Regarding products, LiDAR produces elevation surfaces, digital terrain models (DTM) and digital surface models (DSM). The difference between the DTM and DSM provides a measure of the vertical height of features protruding from the DTM surface such as vegetation and buildings. However, to produce these products, a classification of the points associated with the ground and in some cases hard (buildings) and soft (vegetation) above the ground surface needs to be undertaken (Fig. 8). Following classification, the elevation surfaces can be interpolated to form regularly spaced raster grids. To derive other products from LiDAR, such as gap fraction (e.g.,

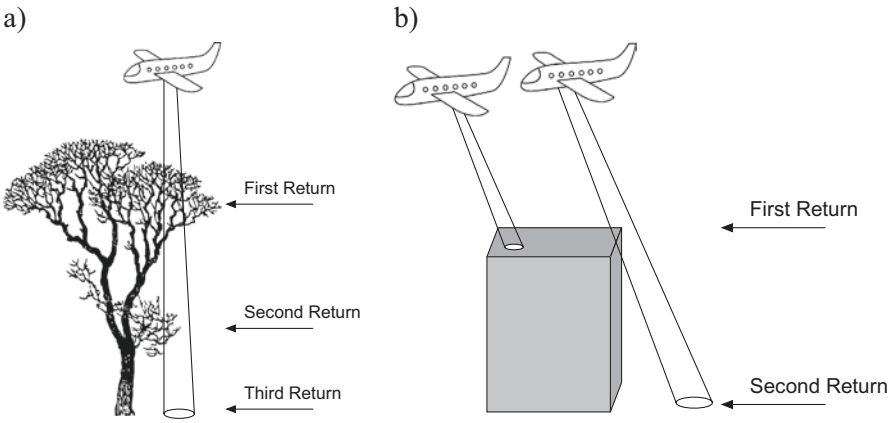

Fig. 7 (**a**) Multiple returns within a vegetation canopy and (**b**) multiple returns from the edge of a building

Armston et al. 2013; Morsdorf et al. 2006), above ground biomass (e.g., Babcock et al. 2016; Popescu 2007; Nelson et al. 1988) and other structural measures (e.g., Palace et al. 2015; Higgins et al. 2014; Zimble et al. 2003), site or region specific relationships are needed. These involve the correlation of LiDAR-derived metrics associated with the vertical structure of the vegetation with ground-based field data.

To undertake LiDAR data processing, dedicated software processing tools are required. LiDAR datasets are typically large and require a reasonable amount of computing power and storage to handle these data. Table 7 lists a number of software packages available for analyzing LiDAR data where LAStools is probably the most popular and widely used providing plugins for both ESRI ArcMap and the QGIS software packages to provide an 'easy to use' environment.

Classification of Point Clouds

To produce a DTM product from LiDAR data, the classification of ground returns and the quality of that classification is a critical processing step. There are many publications demonstrating methods for this task (e.g., Mongus and Zalik 2012; Evans and Hudak 2007; Zhang et al. 2003). However, you will most likely be limited to the algorithms implemented within the processing tools you have available.

The quality of the classification of the ground returns, and therefore the derived DTM, is limited by the number and density of the LiDAR returns that have reached the ground surface. If the LiDAR has not recorded the ground surface, then obviously the ground returns cannot be correctly identified. Where ground returns are very sparse, it is likely that they will be identified as outliers (i.e., noise) rather than true ground returns. Dense vegetation over-stories, particularly those close to the ground (i.e., 1–2 m in height), often limit the number of ground returns. However,

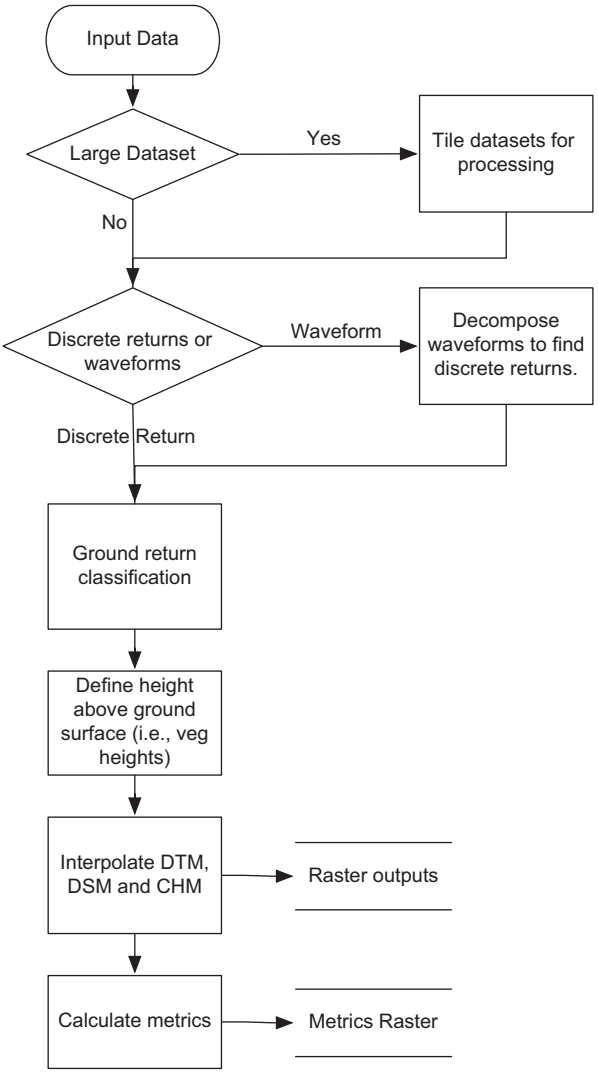

Fig. 8 Flowchart for a standard LiDAR processing chain (Adapted from Bunting et al. 2013)

if known, this can be mitigated by (a) flying higher resolution LiDAR (i.e., the number of pulses per m^2), (b) decreasing the flying height (i.e., more laser power to get weaker ground returns, but this limits the swath width), and (c) using a sensor which can differentiate returns closer to one another along the path of the pulse. Some older instruments can only differentiate returns more than 0.5–1 m from one another along the path of the pulse. Another area where ground returns can be poorly defined or classified is very steep terrain, particularly where there is also vegetation cover (Bater and Coops 2009). It is recommended that for deriving elevation models, at least 4 points per m^2 are acquired but if retrieving the vertical forest structure is of

Table 7 Software for processing LiDAR data

Software	Description	License
LAStools[a]	Becoming the most commonly used tools across the industry providing a wide range of tools. However, the free version is limited.	Commercial & Limited free version.
SPDLib[b]	Tools and file format for common LiDAR processing steps including waveform data.	Open Source
PyLiDAR[c]	A set of python modules enabling easy assesses to the LiDAR (discrete return and waveform) data as numpy arrays allowing implementation of your own algorithms.	Open Source
BCal LiDAR Tools[d]	Widely used tools, written in IDL and used through ENVI.	Open Source
Fusion[e]	US Forestry Service tools, used by many.	Free but closed source
Potree[f]	Tool for visualisation LiDAR on the web	Open Source

[a]http://lastools.org
[b]http://www.spdlib.org
[c]http://www.pylidar.org
[d]https://bcal.boisestate.edu/tools/lidar
[e]http://forsys.cfr.washington.edu/fusion/fusionlatest.html
[f]http://potree.org

interest (e.g., for establishing relationships to forest biomass), then increasing that to 8 points per m^2 is beneficial.

Standard Raster Products

Interpolation of Elevation Surfaces

The resolution at which the raster surface can be interpolated to is dependent on the density of returns that define the surface. Using the Nyquist rate, the density of returns to accurately sample the surface needs to be twice the resolution of the surface being produced to ensure all features are completely represented. However, as the ground return density varies across the scene, a compromise is usually made.

A common requirement for a DTM is that it is hydraulically correct in that it contains no holes or artificial troughs. To ensure hydraulic correctness, algorithms for filling DTM holes are applied and additional information such as break lines (e.g., river shore) can also be included in the interpolation processing.

There are many interpolation algorithms available for the generation of elevation surfaces from point cloud files including Natural Neighbour, Thin Plated Splines, Nearest Neighbour, Linear Triangulation and Inverse Distance Weighted. Bater and Coops (2009) compared a number of these algorithms and demonstrated, for a vegetation-dominated environment, that the Natural Neighbour algorithm produced high-quality results. They recommended this algorithm for general use.

Derivation of Metrics for Vertical Vegetation Structure

There are numerous statistical measures of the vertical distribution of the point cloud that have been used within the literature (e.g., Bunting et al. 2013). These include, the ratio of the number of ground returns to all returns, mean height, median height, mode height, maximum height, standard deviation of all or returns above a certain height, percentiles of height, skewness in height, Pearson mode of height, Pearson median of height and the kurtosis in height. Additionally, by filtering the returns based on their classification (e.g., ground or not-ground) or return number (e.g., first returns) etc., there are many variants of metrics which can be calculated. Your given choice of software tools will enable these metrics to be calculated. For instance, LAStools provides a command line tool to retrieve forestry metrics (lascanopy) while SPDLib provides a tool called spdmetrics. Once calculated, these metrics are commonly used within either a classification scheme to retrieve categorical classes for the scene or used within a regression analysis to field data to retrieve parameters, such as above ground biomass.

Radiometric Correction

There have been a number of attempts to radiometrically correct and/or normalise the LiDAR intensity/amplitude data (e.g., Donoghue et al. 2007). However, as of yet, there are few examples within the literature that demonstrate a clear application for this product. Therefore, for information on these processing stages, the reader is referred to Wagner (2010) and Coren and Sterzai (2007).

Standard Data Specifications

A number of organisations worldwide (e.g., the Intergovernmental Committee on Surveying and Mapping's; http://www.icsm.gov.au/elevation/) have set out standard specifications for the acquisition of LiDAR data. These specifications are commonly regarded as the minimum specification for the organisation. These specifications help ensure that data acquisitions are fit for purpose and can be used to meet the wider requirements of the organisation rather than just specific project needs. Table 8 lists a number of available specifications and, if you are acquiring LIDAR data, reference to these specifications is recommended.

Table 8 LiDAR acquisition specifications

Organisations	Location
ICSM[a]	Australia and New Zealand
British Columbia[b]	Canada
AusCover[c]	Australia
National Network of Regional Coastal Monitoring Programmes of England[d]	UK
USGS[e]	USA

[a]http://www.icsm.gov.au/elevation/
[b]http://geobc.gov.bc.ca/base-mapping/atlas/trim/specs/
[c]http://data.auscover.org.au/xwiki/bin/view/Good+Practice+Handbook/WebHome
[d]http://www.channelcoast.org/national/procurement
[e]https://lta.cr.usgs.gov/lidar_digitalelevation

Synthetic Aperture Radar (SAR)

Overview of SAR

SAR is an active instrument that sends pulses in the microwave region of the electromagnetic spectrum and records the return. The returns are processed in such a way that the movement of the instrument is used to synthesise a larger antenna than would others be physically impossible, which allows a high spatial resolution image to be produced. Forming a SAR image from the raw data is normally carried out by the data provider. The most common product from a SAR is an image of normalised radar cross section or 'backscatter' (σ^0), which is unitless. Partly because of the large range of values, σ^0 is normally expressed on a log scale in decibels (dB). However, depending on the mode and specification of the instrument, other products such as polarimetric decompositions (e.g., Pauli Decomposition; Krogager 1990) can also be generated. Where multiple acquisitions from different geometries are available (i.e., multiple satellite passes), products such as the coherence (Gaveau et al. 2003) and 3D structural information can also be derived (e.g., Ho Tong Minh et al. 2016). However, within this Chapter, just the considerations of the backscatter intensity and SAR, in general, will be discussed. For a full introduction to SAR imagery and processing, refer to Woodhouse (2005).

The intensity of σ^0 is dependent on the vertical structure (i.e., buildings and vegetation) and moisture (predominantly soil). As the size of the vertical structure increases, the magnitude of the SAR backscatter increases. For example, within a forest, pixels of higher backscatter will typical correspond with areas of larger trees. However, the background soil and vegetation moisture can also influence the signal. For example, Lucas et al. (2010) demonstrated that in dry regions of Australia, rain events can increase the SAR backscatter and therefore recommended the use of the driest scenes available when generating regional mosaics. These were identified through reference to spatial interpolations of rainfall measurements or low resolution, high-frequency AMSR-E passive microwave radiometer measures of surface

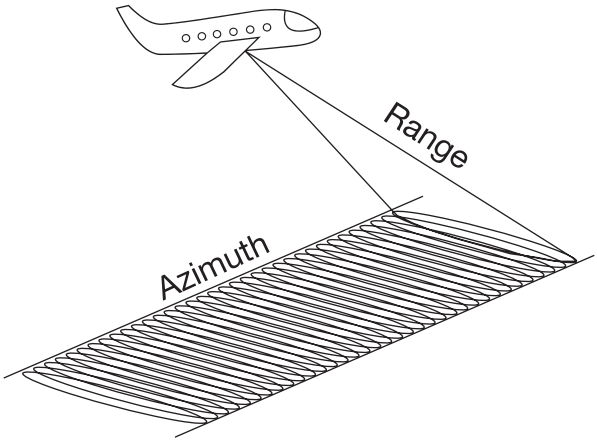

Fig. 9 The side-looking geometry of a SAR system

moisture. Reference to datasets such as these is particularly important where a time series is being constructed as scene(s) or parts of scenes might not be directly comparable in terms of vegetation change as the backscatter changes would correspond with soil and/or surface vegetation moisture amounts.

Geometric Correction

The geometry of a SAR system is quite different from that of an optical or LiDAR in that the sensor is side looking (Fig. 9) and therefore features closer to the sensor will be closer together than those further away in the raw slant-range image space. Therefore, one of the first processing stages within the geometric correction is to convert the slant-range image space into ground-range (i.e., all pixels have an equal ground cover). Following the conversion to ground range, an orthorectification is required to place the SAR imagery into the required geographic coordinate system, with consideration given to topographic relief.

Defining Sigma Nought (σ^0) and Gamma Nought (γ^0)

Typically the pixel values of the ground range images are supplied as digital numbers (DN) (to reduce the file size) and need to be converted to σ^0[dB]. To achieve this, a calibration offset (C) is applied.

$$\sigma^{\mathbf{0}}[dB] = 10\log 10\,(\mathrm{DN}) + C$$

The exact form of the equation to convert from DN to σ^0 varies for each instrument. σ^0 has an angular effect due to the variance in the incidence angles across the scene, particularly for airborne SAR where the variance in incidence angle is higher. Therefore, a correction to γ^0 can also be applied, where θ is the local incidence angle.

$$\gamma^{\mathbf{0}}\left[dB\right] = \mathbf{10}\log 10\left(\frac{\mathrm{DN}}{\theta}\right) + C$$

When using σ^0 [dB] or γ^0 [dB] values for further processing, care is required when applying a process that takes an average or sums any of the pixel values, as dB is a log value. To convert from dB use:

$$\sigma^{\mathbf{0}} = \mathbf{10}\left(\frac{\sigma^0\left[dB\right]}{10}\right)$$

Following any calculations, for example calculating a mean backscatter for a set of image segments, dB values can be retrieved using:

$$\sigma^{\mathbf{0}}\left[dB\right] = \mathbf{10}\log 10\left(\sigma^0\right)$$

SAR Image Filtering

SAR images contain speckle, which is noise from the image acquisition process. To reduce speckle within the scene image, filters are commonly used. Filters can be applied to a single image (e.g., Lee Filter; Lee 1981) or to time-series (Trouve et al. 2003). It is commonly recommended (Woodhouse 2005) that speckle filters are applied to SAR imagery before it is used unless the image data is being smoothed (averaged) in some way, which is the case when segmentation procedures are applied.

Conclusions

This chapter has attempted to provide an brief but wide ranging overview of the methods and processes that need to be considered when receiving remote sensing imagery prior to using the imagery for your application of interest. Once these processes are applied, the image data can be considered as analysis ready. Without satisfying the requirement of an ARD product prior to undertaking your application, is likely that your analysis will either fail or produce suboptimal results.

The deviation of ARD products can be undertaken by yourself if you have the appropriate background knowledge and software tools. However, the data provider(s) or other organisations or individuals can provide services to derive these products.

References

Armston, J., Disney, M.I., Lewis, P., Scarth, P., Phinn, S., Lucas, R.M., Bunting, P., Goodwin, N.: Direct retrieval of canopy gap probability using airborne waveform lidar. Remote Sens. Environ. **134**, 24–38 (2013)

Babcock, C., Finley, A.O., Cook, B.D., Weiskittel, A., Woodall, C.W.: Modeling forest biomass and growth: coupling long-term inventory and LiDAR data. Remote Sens. Environ. **182**, 1–12 (2016)

Bater, C., Coops, N.: Evaluating error associated with lidar-derived DEM interpolation. Comput. Geosci. **35**(2), 289–300 (2009)

Bunting, P., Armston, J., Clewley, D., Lucas, R.M.: Sorted pulse data (SPD) library—part II: a processing framework for LiDAR data from pulsed laser systems in terrestrial environments. Comput. Geosci. **56**, 207–215 (2013)

Chavez Jr., P.S.: An improved dark-object subtraction technique for atmospheric scattering correction of multispectral data. Remote Sens. Environ. **24**(3), 459–479 (1988)

Claverie, M., Vermote, E.F., Franch, B., Masek, J.G.: Evaluation of the Landsat-5 TM and Landsat-7 ETM+ surface reflectance products. Remote Sens. Environ. **169**, 390–403 (2015)

Coren, F., Sterzai, P.: Radiometric correction in laser scanning. Int. J. Remote Sens. **27**(15), 3097–3104 (2007)

Draper, D.W., Newell, D.A., Wentz, F.J., Krimchansky, S., Skofronick-Jackson, G.M.: The Global Precipitation Measurement (GPM) Microwave Imager (GMI): Instrument Overview and Early On-Orbit Performance. Sel. Top. Appl. Earth Obs. Remote Sens. IEEE J. **8**(7), 3452–3462 (2015.) http://doi.org/10.1109/JSTARS.2015.2403303

Donoghue, D.N.M., Watt, P.J., Cox, N.J., Wilson, J.: Remote sensing of species mixtures in conifer plantations using LiDAR height and intensity data. Remote Sens. Environ. **110**(4), 509–522 (2007)

Frantz, D., Röder, A., Stellmes, M., Hill, J.: An operational radiometric landsat preprocessing framework for Large-Area time series applications. IEEE Trans. Geosci. Remote Sens. 1–16 (n.d..) http://doi.org/10.1109/TGRS.2016.2530856

Evans, J.S., Hudak, A.T.: A multiscale curvature algorithm for classifying discrete return LiDAR in forested environments. IEEE Trans. Geosci. Remote Sens. **45**(4), 1029–1038 (2007)

Feng, M., Sexton, J.O., Huang, C., Masek, J.G., Vermote, E.F., Gao, F., et al.: Global surface reflectance products from Landsat: assessment using coincident MODIS observations. Remote Sens. Environ. **134**, 276–293 (2013)

Gaveau, D.L.A., Balzter, H., Plummer, S.: Forest woody biomass classification with satellite-based radar coherence over 900 000 km2 in Central Siberia. For. Ecol. Manag. **174**(1–3), 65–75 (2003)

Green, M., Kondragunta, S., Ciren, P., Xu, C.: Comparison of GOES and MODIS Aerosol Optical Depth (AOD) to Aerosol Robotic Network (AERONET) AOD and IMPROVE PM2.5 Mass at Bondville, Illinois. J. Air Waste Manage. Assoc. **59**(9), 1082–1091 (2009)

Higgins, M.A., Asner, G.P., Martin, R.E., Knapp, D.E., Anderson, C., Kennedy-Bowdoin, T., Saenz, R., Aguilar, A., Wright, S.J.: Linking imaging spectroscopy and LiDAR with floristic composition and forest structure in Panama. Remote Sens. Environ. **154**, 358–367 (2014)

Ho Tong Minh, D., Le Toan, T., Rocca, F., Tebaldini, S., Villard, L., Réjou-Méchain, M., Phillips, O.L., Feldpausch, T.R., Dubois-Fernandez, P., Scipal, K., Chave, J.: SAR tomography for the retrieval of forest biomass and height: cross-validation at two tropical forest sites in French Guiana. Remote Sens. Environ. **175**, 138–147 (2016)

Jhan, J.-P., Rau, J.-Y., Huang, C.-Y.: Band-to-band registration and ortho-rectification of multilens/multispectral imagery: a case study of MiniMCA-12 acquired by a fixed-wing UAS. ISPRS J. Photogramm. Remote Sens. **114**, 66–77 (2016)

Ju, J., Roy, D.P., Vermote, E., Masek, J., Kovalskyy, V.: Continental-scale validation of MODIS-based and LEDAPS Landsat ETM+ atmospheric correction methods. Remote Sens. Environ. **122**, 175–184 (2012)

Krogager, E.: New decomposition of the radar target scattering matrix. Electron. Lett. **26**(18), 1525–1527 (1990)

Lee, J.-S.: Speckle analysis and smoothing of synthetic aperture radar images. Comput. Graph. Image Process. **17**(1), 24–32 (1981)

Lillesand, T.M., Kiefer, R.W., Chipman, J.W.: Remote Sensing and Image Interpretation, 5th edn. Wiley, Hoboken (2004)

Lucas, R., Armston, J., Fairfax, R., Fensham, R., Accad, A., Carreiras, J., Kelley, J., Bunting, P., Clewley, D., Bray, S., Metcalfe, D., Dwyer, J., Bowen, M., Eyre, T., Laidlaw, M., Shimada, M.: An evaluation of the ALOS PALSAR L-Band backscatter – above ground biomass relationship Queensland, Australia: impacts of surface moisture condition and vegetation structure. Sel. Top. Appl. Earth Obs. Remote Sens. IEEE J. **3**(4), 576–593 (2010)

Masek, J.G., Vermote, E.F., Saleous, N.E., Wolfe, R., Hall, F.G., Huemmrich, K.F., et al.: A Landsat surface reflectance dataset for North America, 1990–2000. Geosci. Remote Sens. Lett. IEEE. **3**(1), 68–72 (2006)

Mongus, D., Zalik, B.: Parameter-free ground filtering of LiDAR data for automatic DTM generation. ISPRS J. Photogramm. Remote Sens. **67**, 1–12 (2012)

Morsdorf, F., Kötz, B., Meier, E., Itten, K.I., Allgöwer, B.: Estimation of LAI and fractional cover from small footprint airborne laser scanning data based on gap fraction. Remote Sens. Environ. **104**(1), 50–61 (2006)

Nagol, J.R., Sexton, J.O., Kim, D.-H., Anand, A., Morton, D., Vermote, E., Townshend, J.R.: Bidirectional effects in Landsat reflectance estimates: is there a problem to solve? ISPRS J. Photogramm. Remote Sens. **103**, 129–135 (2015)

Nelson, R., Krabill, W., Tonelli, J.: Estimating forest biomass and volume using airborne laser data. Remote Sens. Environ. **24**(2), 247–267 (1988)

Palace, M.W., Sullivan, F.B., Ducey, M.J., Treuhaft, R.N., Herrick, C., Shimbo, J.Z., Mota-E-Silva, J.: Estimating forest structure in a tropical forest using field measurements, a synthetic model and discrete return lidar data. Remote Sens. Environ. **161**, 1–11 (2015)

Popescu, S.C.: Estimating biomass of individual pine trees using airborne lidar. Biomass Bioenergy. **31**(9), 646–655 (2007)

Roy, D.P., Ju, J., Kline, K., Scaramuzza, P.L., Kovalskyy, V., Hansen, M., et al.: Web-enabled Landsat Data (WELD): Landsat ETM+ composited mosaics of the conterminous United States. Remote Sens. Environ. **114**(1), 35–49 (2010)

Schlapfer, D., Richter, R.: Geo-atmospheric processing of airborne imaging spectrometry data. Part 1: parametric orthorectification. Int. J. Remote Sens. **23**(13), 2609–2630 (2002)

Schwind, P., Schneider, M., Palubinskas, G., Storch, T., Mueller, R., Richter, R.: Processors for ALOS optical data: Deconvolution, DEM generation, Orthorectification, and atmospheric correction. Geosci. Remote Sens. IEEE Trans. **47**(12), 4074–4082 (2009)

Shan, J., Toth, C.K.: Topographic Laser Ranging and Scanning: Principles and Processing. CRC Press, Boca Raton (2009)

Smith, G.M., Milton, E.J.: The use of the empirical line method to calibrate remotely sensed data to reflectance. Int. J. Remote Sens. **20**, 2653–2662 (2010)

Trouve, E., Chambenoit, Y., Classeau, N., Bolon, P.: Statistical and operational performance assessment of multitemporal SAR image filtering. Geosci. Remote Sens. IEEE Trans. **41**(11), 2519–2530 (2003)

Vermote, E.F., Tanre, D., Deuze, J.L., Herman, M., Morcette, J.J.: Second simulation of the satellite signal in the solar Spectrum, 6S: an overview. Geosci. Remote Sens. IEEE Trans. **35**(3), 675–686 (1997)

Wagner, W.: Radiometric calibration of small-footprint full-waveform airborne laser scanner measurements: basic physical concepts. ISPRS J. Photogramm. Remote Sens. **65**(6), 505–513 (2010)
Wilson, R.T., Milton, E.J., Nield, J.M.: Spatial variability of the atmosphere over southern England, and its effect on scene-based atmospheric corrections. Int. J. Remote Sens. **35**(13), 5198–5218 (2014)
Woodhouse, I.H.: Introduction to Microwave Remote Sensing. CRC Press, Boca Raton (2005)
Zimble, D.A., Evans, D.L., Carlson, G.C., Parker, R.C., Grado, S.C., Gerard, P.D.: Characterizing vertical forest structure using small-footprint airborne LiDAR. Remote Sens. Environ. **87**(2–3), 171–182 (2003)
Zhang, K., Chen, S., Whitman, D., Shyu, M., Yan, J., Zhang, C.: A progressive morphological filter for removing nonground measurements from airborne LIDAR data. IEEE Trans. Geosci. Remote Sens. **41**(4), 872–882 (2003)
Zwally, H.J., Schutz, B., Abdalati, W., Abshire, J., Bentley, C., Brenner, A., Bufton, J., Dezio, J., Hancock, D., Harding, D., Herring, T., Minster, B., Quinn, K., Palm, S., Spinhirne, J., Thomas, R.: ICESat's laser measurements of polar ice, atmosphere, ocean, and land. J. Geodyn. **34**(3–4), 405–445 (2002)